

Prospects for Constraining Cosmological Parameters using Future Detectors - 431

Student Number: 2064198

Abstract. Observations suggest we live in a geometrically flat universe, or at least, close to flat. The Cosmic Microwave Background Radiation (CMBR) confirms this by constraining the curvature parameter to an error of as little as $\sigma_{\Omega_k} = 0.002$. The aim of this project is to determine the observations of Type Ia Supernovae (SNeIa) and Massive Binary Black Hole Mergers (MBBHM) required to be able to distinguish between a flat, hyperbolic, or spherical universe within this variance. If successful, these observations will provide an alternative means of constraining the curvature parameter and if they match current observations of the CMBR, we gain confidence in the current concordance model of the Universe. The recent developments in gravitational wave astronomy have opened a new door for precision cosmology with high potential for achieving the aim of further constraining the curvature parameter. To model this potential, firstly mock supernovae data is generated to understand the number of observations required to achieve the target degree of precision. The same process is then followed to create datasets which could be expected from the gravitational wave signature of MBBHM systems, these are further refined to incorporate the effect of gravitational weak lensing to demonstrate how this has an impact on achieving the desired accuracy of the data. Analysis suggests that an optimistic outlook on future observation will yield an error level of $\sigma_{\Omega_k} = 0.0036$, a factor of two larger than that given by the CMBR. The combination of further searches and the use of other probes shows promise for reducing this variance level.

1. Introduction

1.1. General relativity and the expanding Universe

The theory of General Relativity (GR), formulated by Einstein in 1915, is a geometric theory of gravitation that, in essence, describes the effect of matter and energy on the curvature of space-time, along with the effect of the curvature of space-time on matter and energy. It unifies the theory of special relativity and Newtonian gravitation which allows accurate predictions of motion, generally on large scales. This also applies to the very large scale and hence can be used to create predictions of how the Universe evolves over time. Within his field equations, Einstein added an additional term, called the cosmological constant, providing a negative pressure which would allow for a static universe to match observations at the time. Shortly after, it was shown independently by Alexander Friedmann and Georges Lemaître, that any small perturbation would throw this static universe into a dynamic one [1]. This was then confirmed in 1929 by Edwin Hubble through the observation of the nearby galaxies, when he noticed that the greater the distance to the galaxy, the greater its recession velocity - now known as the Hubble-Lemaître law. What he concluded from this is that the Universe is expanding, and at a rate of $570\text{kms}^{-1}\text{Mpc}^{-1}$ (a massive overestimation due to peculiar velocities of galaxies). This observation went directly against Einstein's prediction of a static universe and resulted in Einstein withdrawing the cosmological constant and calling it his "biggest blunder".

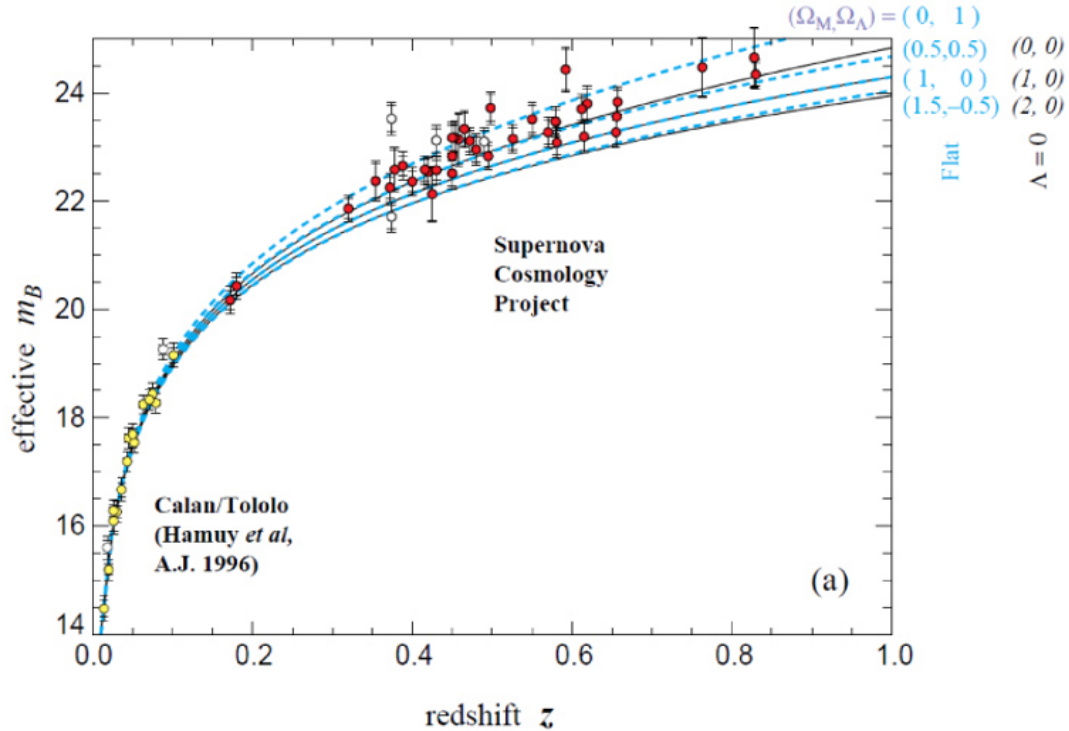


Figure 1. Hubble diagram plotting 42 high redshift supernova from the Supernova Cosmology Project (red) and 18 low redshift supernova from the Calán/Tololo Supernova Survey (yellow), the unfilled points are supernovae excluded from the fit. Dashed lines represent predictions using different models of a flat universe. A best fit is given by a flat universe with $\Omega_M = 0.28$ and $\Omega_\Lambda = 0.72$. Figure taken from Perlmutter [2].

1.2. Accelerated expansion and Λ CDM

A relatively recent discovery made by two teams of independent astronomers led by Saul Perlmutter [2], and Brian P. Schmidt with Adam G. Riess [3], through the observation of highly redshifted SNeIa, concluded that after an initial phase of deceleration in the early Universe (when matter density was high), the Universe has recently transitioned into a phase of cosmic acceleration. This suggests that there is a component in the Universe which has the opposite effect of gravity. Taking the theory of general relativity to be true, the Universe consists of matter and radiation with mass slowing the expansion and radiation driving it. We must therefore be missing a key component which is driving this accelerated expansion, something that could be conveniently explained by Einstein's cosmological constant. This leads to our current best description of the Universe, Λ CDM, otherwise known as the concordance model, which describes a universe filled with dark energy, and cold dark matter which gives the best explanation for the structure of the CMBR. Within this model we can describe the expansion of the Universe with several different parameters; the curvature density, dark energy density, and matter density and the model currently predicts the weighting of these to be 0, 0.7, and 0.3, respectively. The curvature density quantifies the overall geometry of space, being either spherical, Euclidean, or hyperbolic - the 2-dimensional analogues are illustrated in figure 2. The dark energy density describes the component of the Universe which provides the negative pressure, and in turn, the currently observed accelerated expansion. Explanations of this elusive component remain a mystery with predictions such as an intrinsic vacuum energy through the Heisenberg uncertainty principle providing an energy component orders of magnitude larger than observed. Finally, we

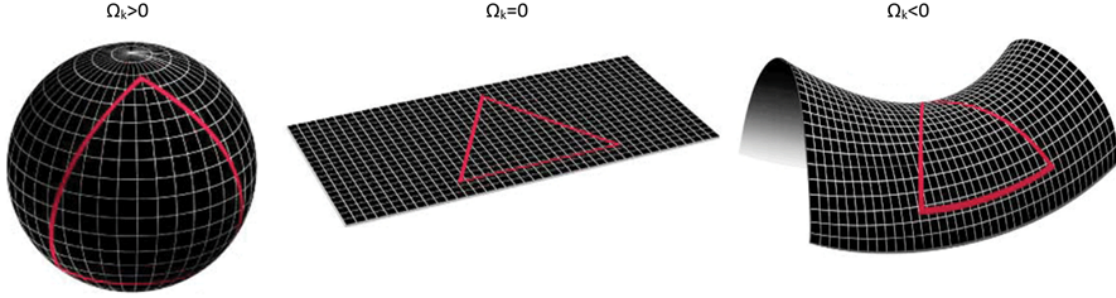


Figure 2. Graphical representation of two-dimensional analogues of universe geometries. Left shows a spherical universe with $\Omega_k > 1$, parallel rays of light will converge. Middle shows a Euclidean universe with $\Omega_k = 0$, parallel rays of light will remain so. Right shows a hyperbolic universe with $\Omega_k < 0$, parallel rays of light will diverge.

have the matter density, consisting of both baryonic matter and non-baryonic dark matter which, depending on its relative abundance, slows the expansion of the Universe.

Much of modern cosmology is based on constraining these parameters, and others. There are currently many probes which allow for such possible constraints to be made, the most successful of these include; anisotropies in the Cosmic Microwave Background Radiation (CMBR), Baryon Acoustic Oscillations (BAO), type Ia Supernovae (SNeIa), and with recent developments in gravitational wave detectors, Binary Black Hole Mergers (BBHM). This project will focus on the use of SNeIa as standard candles and BBHMs as standard sirens to constrain the curvature parameter.

1.3. Cosmological probes

The best current prediction of the geometry of space has come primarily from looking at the CMBR. It is the oldest optically observable remnant of the Universe stretching back to the epoch of recombination ($\sim 400,000$ years after the Big Bang), at which point the baryon-photon plasma of the early Universe condensed allowing light to travel freely. Within the CMBR tiny fluctuations appear in its temperature which have been caused by quantum fluctuations. Since the physics behind these fluctuations is well understood, it is possible by inference from the angular size of these regions to find the geometry of the Universe. Much like measuring the angles on a curved/flat surface, the angular size of these regions will indicate the curvature of the Universe - smaller regions imply a positive curvature, and larger imply a negative curvature. Three missions have made such measurements possible; COBE, WMAP and Planck, with Planck's survey shown on figure 3. The latter has successfully constrained the curvature parameter to a value of $\Omega_k = 0.0010 \pm 0.002$ [4].

Type Ia Supernovae are known to be one of the most energetic events in the Universe. They are thought to occur when an accreting white dwarf surpasses the Chandrasekhar mass limit, at which point electron degeneracy pressure is no longer strong enough to support the star's own mass. The resultant collapse releases a huge burst of light which generally outshines its host galaxy. This, along with the fact that its peak brightness is correlated to its rate of change in brightness, i.e. less luminous supernovae also fade more quickly, make SNeIa a useful standard candle. Despite this, there are a multitude of errors associated with the detection of SNeIa. These include; extinction, gravitational weak lensing, evolution, and selection effects which make SNeIa slightly less desirable as standard candles [5].

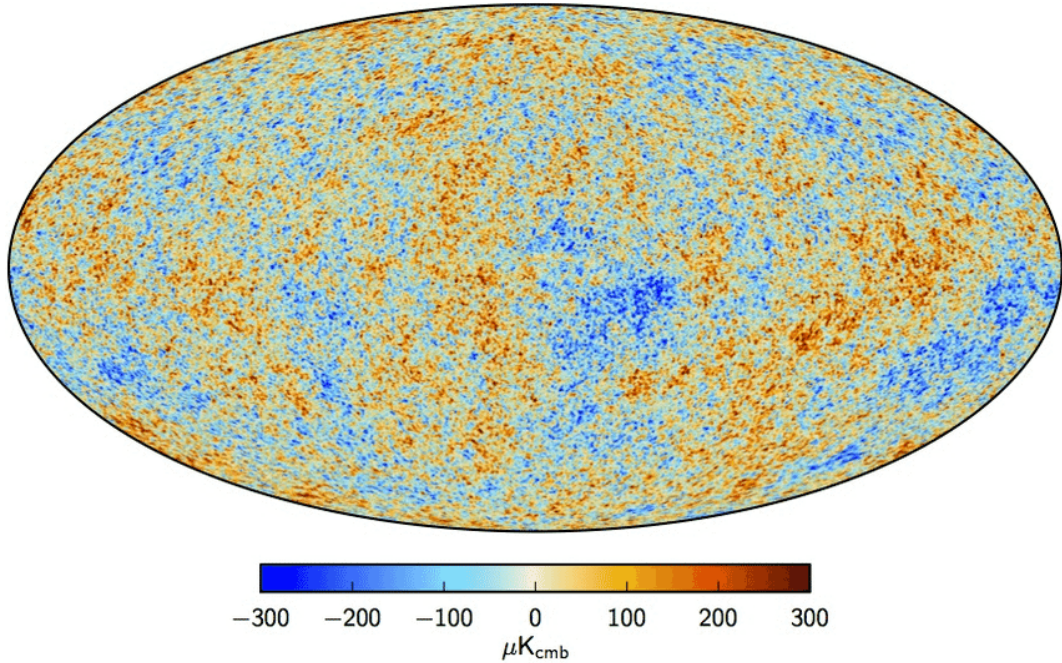


Figure 3. Temperature anisotropies in the CMBR as measured by Planck. Fluctuations have characteristic size which can be used to constrain the curvature density with high precision. Figure taken from ESA and the Planck Collaboration.

The detection of gravitational waves in 2015 (GW150914) [6] produced by a binary black hole merger (BBHM) by the Laser Interferometer Gravitational-wave Observatory (LIGO) has opened a whole new window in observational astronomy. This discovery confirmed Einstein’s prediction of such events through the theory of General Relativity, in which a coalescing BBHM produces a characteristic signal otherwise known as a “chirp”. This however comes with a caveat; the signal produced has mass-redshift degeneracy, meaning we cannot distinguish between a low mass-low redshift source and a high mass-high redshift source for the signal by itself. Hence, we must observe an electromagnetic counterpart which can give us the redshift and break the degeneracy. This can be done in several different ways; locating the host galaxy in which the BBHM occurred will allow redshift measurements of the galaxy (this may be difficult since current observatories are able to produce measurements with an average error in location of $\sim 60\text{deg}^2$ [7]), or to measure the emission produced for the merger itself (neutron star-neutron star mergers and MBBHM are targets for these). This will then allow an estimation of the sources’ mass and luminosity distance, all with very minimal uncertainties since the gravitational waves will only interact with objects gravitationally.

1.4. Future missions

This project focuses on the predicted observations to be made by two missions, namely, The Large Synoptic Survey Telescope (LSST), and the Laser Interferometer Space Antenna (LISA). LSST is a wide field telescope which will measure most of the observable sky over six optical bands, every few nights. The fact that such a large portion of the sky will be surveyed so frequently makes it ideal for the observations of SNeIa and the mission expects to observe hundreds of thousands of such events over its ten year programme [8]. This mission itself provides us with a good approximation for an upper boundary of the number of objects to be observed in the near future. One of the challenges that comes with LSST is that it uses photometric

measurements of redshift which will have associated errors unlike spectroscopic measurements. The process for estimating these errors will be covered in section 4.1. LISA is a proposed space-based interferometer with a proposed arm length of 2.5 million km. This will allow LISA to peer into the low frequency emission of gravitational waves allowing for the detection of thousands of stellar mass BBHMs and many MBBHMs with incredibly high precision [9].

2. Basic Equations

This section provides an overview of the main equations of the underlying physics involved in this project. It will largely cover the equations associated with the cosmologies as well as how the distance to a source is inferred, but will not go into the complex physics involved with the production of supernovae and gravitational waves.

2.1. Cosmology

In this project we assume Einstein's theory General relativity and thus a homogeneous and isotropic universe. In which, spacetime is described by the Friedmann-Lemaître-Robertson-Walker (FLRW) metric [1]

$$ds^2 = dt^2 - a^2(t) \left[\frac{dr^2}{1 - kr^2} + r^2 d\theta^2 + r^2 \sin^2 \theta d\phi^2 \right], \quad (1)$$

where k describes the curvature of space, $a(t)$ is the cosmic scale factor - a ratio of the proper distance and co-moving distance, and r, θ, ϕ are spatial coordinates. This is important since the scale factor will be used to infer the luminosity-distance of objects at a specific redshift. Combining the FLRW metric with Einstein's field equations produces the Friedmann equations [1]

$$H^2 = \left(\frac{\dot{a}}{a} \right)^2 = \frac{8\pi G\rho}{3} - \frac{k}{a^2} + \frac{\Lambda}{3} \quad (2)$$

$$\frac{\ddot{a}}{a} = \frac{-4\pi G}{3}(\rho + 3p) + \frac{\Lambda}{3}, \quad (3)$$

where H is the Hubble constant, defined by $H \equiv \dot{a}/a$, G is the gravitational constant, ρ is the energy density of the Universe including matter, radiation and dark energy, and p is the pressure from all these components combined. These equations together, describe the evolution and expansion of space in a FLRW metric. We can take equation 2 to produce the dimensionless density parameters; matter density, spatial curvature density, and dark energy density respectively

$$1 = \frac{8\pi G\rho}{3H^2} - \frac{k}{a^2 H^2} + \frac{\Lambda}{3H^2} = \Omega_m + \Omega_k + \Omega_\Lambda. \quad (4)$$

The matter density, Ω_m , is the contribution of all baryonic and non-baryonic matter, which through gravity, exerts a force pulling the Universe together. In a Λ CDM model this takes a value of 0.3. Of this, a mere 0.04 comes from baryonic matter (i.e the matter we can physically observe such as stars and planets) and the rest from non-baryonic in the form of dark matter. These values are inferred mainly from gravitational lensing of galaxies as well as the kinematics of galaxies. Ω_Λ refers to the dark energy density of the Universe, which contributes a negative pressure hence accelerating the expansion of the Universe. It takes a value of $\Omega_\Lambda = 0.7$. This leaves the spatial curvature density which, as mentioned before, defines the geometry of space. In the Λ CDM model this takes a value of $\Omega_k = 0$, corresponding to a flat universe.

In a universe in which the expansion rate varies over time, the Hubble constant does not apply and the Hubble parameter, $H(z)$, must be used instead. This can be written in dimensionless form

$$E(z) = \sqrt{\Omega_m(1+z)^3 + \Omega_\Lambda + \Omega_k(1+z)^2}, \quad (5)$$

where H_0 is the Hubble constant at $z = 0$. Here, we can see the dependence on the different density parameters; mass dominates at large redshifts, whereas dark energy only recently has a significant effect.

2.2. Distance measurements

To determine the distance to an object at redshift z , we must integrate from $z = 0$ to the object over the infinitesimal contributions of the local Hubble parameter from equation 5, multiplied by the Hubble distance, $d_H \equiv c/H_0$, where c is the speed of light in a vacuum, H_0 is the Hubble constant. This gives us what is called the line of sight co-moving distance [10]

$$d_C(z) = \frac{c}{H_0} \int_0^z \frac{dz'}{E(z')}. \quad (6)$$

This can be used to give us the transverse co-moving distance, [10]

$$d_M(z) = \begin{cases} \frac{c}{H_0 \sqrt{|\Omega_k|}} \sin\left(\int_0^z \frac{dz'}{E(z')}\right), & \Omega_k < 0 \\ d_C(z), & \Omega_k = 0 \\ \frac{c}{H_0 \sqrt{|\Omega_k|}} \sinh\left(\int_0^z \frac{dz'}{E(z')}\right), & \Omega_k > 0 \end{cases} \quad (7)$$

where the co-moving distance between two objects at the same redshift separated by an angular diameter, $\delta\theta$, is $d_M\delta\theta$.

Standard luminosity distance to a source with a known luminosity and flux is given by

$$d_L = \sqrt{\frac{L}{4\pi F}}. \quad (8)$$

Since the distance to a source with expanding space between the object and observer is being considered, the distance luminosity to a source as a function of redshift, z , is given by [10]

$$d_L = (1+z)d_M \quad (9)$$

This set of equations now allows us to infer cosmological parameters by constructing $d_L - z$ diagrams based on a set of cosmological parameters and comparing it to that produced by real observed objects. We can now convert this distance measurement into distance modulus using

$$\mu_m = 5\log(d_L) + 25. \quad (10)$$

This quantifies the relative relative brightness of a source of known luminosity and will be important later on.

2.3. Statistical Analysis

This section covers the relevant areas of statistical analysis covering firstly the frequentist approach of χ^2 minimisation, followed by the Bayesian method applied using a Markov Chain Monte Carlo (MCMC) method.

Frequentist statistics involves the process of obtaining probabilities using a large sample of measurements. This is applicable for a large data set since the relative frequency of a

specific outcome approaches its true probability value as the number of samples in the data set approaches infinity. This method can be applied to many areas in physics, especially particle physics where millions of events occur, but is also applicable to cosmological data sets. Consider a set of N data points, $\mathcal{D} = \{x_1, x_2, \dots, x_N\}$, with an error, σ_i , associated with each measurement. We can fit a model, M , defined by a set of J parameters, $\lambda = \{\lambda_1, \lambda_2, \dots, \lambda_J\}$, by defining a likelihood function as the probability of the observed data as a function of these parameters. Assuming the data is Gaussian, this follows as [11]

$$p(\mathcal{D}|\lambda) = \frac{1}{\sqrt{2\pi}\sigma} \exp(-\frac{1}{2}\chi^2), \quad (11)$$

where the χ^2 statistic is given by

$$\chi^2 = \sum_{i=0}^N \left(\frac{x_i - x(\lambda)_i}{\sigma_i} \right)^2. \quad (12)$$

To find the best model to fit a given data set, we want to maximise the likelihood function. From equation 11 it can be seen this is achieved by minimising the χ^2 function, i.e finding a set of parameters, λ , which result in the smallest total difference between all the observed and corresponding predicted values.

Bayesian probability differs from Frequentist in the fact that we do not base our entire outcome purely on the given data set, and hence introduce a prior which is proposed from some reasonable starting knowledge. To start, we need to define a joint probability of two events, A and B , occurring, $p(A, B)$, and the conditional probability, $p(A|B)$, which is the probability of A occurring given that B has occurred. The conditional probability can be defined in terms of the joint probabilities,

$$p(A|B) = \frac{p(A, B)}{p(B)}. \quad (13)$$

We can write the equivalent for $p(B|A)$, and using the transitivity of joint probability, $p(A, B) = p(B, A)$, we get to Bayes' theorem:

$$p(A|B) = \frac{p(B|A)p(A)}{p(B)}. \quad (14)$$

Consider, as before, a set of N data points and a model defined by a set of parameters. We can write Bayes' theorem as

$$p(\lambda|\mathcal{D}) = \frac{p(\mathcal{D}|\lambda)p(\lambda)}{p(\mathcal{D})}, \quad (15)$$

where $p(\lambda|\mathcal{D})$ is the posterior, giving the probability of a set of unknown parameters given some data. This is the key value which is to be determined since it allows us to obtain the probability of a set of parameters being the "correct" ones. $p(\mathcal{D}|\lambda)$ is the likelihood which, as mentioned before, is the main point of interest for a Frequentist approach, and is defined in a Gaussian model by equation 11. We then have the prior, $p(\lambda)$, which quantifies any initial beliefs we have on a particular set of parameters. Finally, $p(\mathcal{D})$ is the evidence, but can be ignored in parameter estimation since it factors out as a constant. This idea encompasses that of a Frequentist approach but results in a posterior which combines the result of our parameter estimation from the likelihood along with any prior knowledge of the parameter set.

3. Numerical Methods

This section develops the basic equations discussed in the previous section and explains how these are processed numerically. First we will touch on how distance measurements are calculated, followed by a more in depth description of parameter estimation. All codes developed can be found on: <https://github.com/RyanProbyn52/ParamEst>.

3.1. Distance measurements

Looking at equation 9, we see that the calculation involving distances has an integral. Since the equation does not have an obvious analytical solution we need to evaluate the integral numerically. This can be done in one of many ways and was initially evaluated as a Riemann sum

$$\int_0^z \frac{dz'}{E(z')} \approx \sum_{i=0}^N \frac{\Delta_{width}}{E(z)}, \quad (16)$$

which instead finds the area under the function by finding the value at an interval defined by $N\Delta_{width}$, where $\Delta_{width} = z_{max}/N$. This approaches the analytical solution in the limit as $N \rightarrow \infty$. This however proved to be a relatively slow approach computationally and so an inbuilt scypy function was used instead as it employs a much more efficient and accurate Clenshaw–Curtis quadrature technique.

To further decrease computation time (especially for a large number of objects), another integral approximation was used. Consider any continuous function, $f(x)$, for any range which this function is valid over we can sample N evenly spaced x values to produce N coordinates on the function. We can then draw straight lines between neighbouring points which will approximate the distance luminosity function. Now rather than integrating from $0 \rightarrow z_i$ for every i^{th} object, we can simply integrate once from $0 \rightarrow z_{max}$, and sample the distance luminosity depending on which line segment the z value falls under.

3.2. Statistical analysis

The aim of Bayesian statistics for parameter estimation is to determine the posterior distribution of a model with parameters, $\lambda = \{\lambda_1, \lambda_2, \dots, \lambda_J\}$, and measurements, $\mathcal{D} = \{x_1, x_2, \dots, x_N\}$. We can determine this posterior function by sampling an J -dimensional grid, i.e. for a grid size of 100 and only one parameter to be evaluated, only 100 posterior distributions are calculated. This however increases exponentially since for the same 100 grid points, a J -dimensional model will require 100^J evaluations. If we consider a large data sets where the posterior distribution takes, say, 5 seconds to compute, a 6-dimensional model would take ~ 160 thousand years to compute. However, this project will focus on calculation of a 2-dimensional model (parameters Ω_k and Ω_l), which means this approach is feasible for small data sets consisting of several hundred data points.

To solve the problem of high computation times we can implement a Markov Chain Monte Carlo (MCMC). Rather than sampling an entire grid, a MCMC uses randomly generated points in the parameter space to converge to the highest likelihood value (lowest χ^2) in a gradient descent. This allows for a point of maximum likelihood to be calculated but does not identify the overall posterior distribution to be determined. In effect, we can instead use randomly chosen initial points with which we calculate the χ^2 value. The program will then generate a random point around that initial point at a set proposal density (distance from initial point) and calculate the new χ^2 value. If the new value is less than the previous, it will automatically accept the point, otherwise the new point will be rejected. This process continues until the algorithm finds a the point of maximum likelihood. If we want to sample the overall posterior distribution we can employ a random-walk Metropolis-Hastings (MH) algorithm. This algorithm utilises an additional step within the rejection phase of the new point. This is done by taking the log-likelihood for each point which compares previous χ^2 value to current one, defined such that continuous samples will numerically approximate the posterior distribution. We then generate a random number between 0 and 1 and if the log-likelihood value is greater than the randomly generated number the new point will be accepted. This means that the greater the ratio between the two previous points the greater the probability that the new point will be accepted. An outline of the process is as follows:

- (i) Generate a random point in the parameter space, λ_r (usually around point of maximum likelihood), and set a proposal density for each parameter in λ_r .
- (ii) Evaluate the likelihood the point, $p(\mathcal{D}|\lambda_r)$.
- (iii) Generate a new point around previous point, λ_s , using proposal density, and calculate likelihood at this point, $p(\mathcal{D}|\lambda_s)$.
- (iv) Define log-likelihood ratio as

$$R = \log p(\mathcal{D}|\lambda_s) - \log p(\mathcal{D}|\lambda_r) = 0.5(\chi_r^2 - \chi_s^2), \quad (17)$$

where we use equation 11 for the second equality.

- (v) If $R \geq 0$, accept new point, with $\lambda_{r+1} = \lambda_s$.
- (vi) Otherwise accept new point with probability $\exp(R)$, i.e. $\lambda_{r+1} = \lambda_s$, and reject with probability $1 - \exp(R)$, i.e. $\lambda_{r+1} = \lambda_r$.

After the MCMC has completed, we can sort the array of χ^2 values into order and by plotting the first 68% of the values corresponding to 1σ confidence, 68% – 95% for 2σ and 95% – 99.7% for 3σ , and produce a confidence plot for the estimated parameters, e.g. as seen in figure 6.

There are several important initial values to consider when generating a posterior distribution from a MCMC. Firstly, the proposal density is important; too small a value means that the chain will not explore the appropriate parameter space, too large a value would result in the MCMC getting stuck at the maximum likelihood since the change in likelihood will produce a large negative value, meaning $\exp(R) \ll 1$, resulting in most points being rejected. Secondly, the initial starting point, λ_r , which for this project was solved easily, since the mock data was produced on an assumed model, hence the parameters used in this model would result in the point of maximum likelihood. Finally, the number of points in the chain was important; too few and the MCMC would not accurately represent the posterior distribution, too many could unnecessarily increase computation time.

3.3. Inverse cdf method

This method allows for pseudo-random number sampling and its use is appropriate for generating mock data. For this we take a cumulative distribution function (cdf), say $y = f(z)$, which maps a range of numbers to a probability between 0 and 1, and take the inverse of this function. This will allow for any number to be generated according to the initial distribution by sampling $y \sim U[0, 1]$, a uniform sample between 0 and 1. However, most cdfs do not have an analytical inverse. A simple solution to this is to approximate the cdf as a multitude of small line segments. Similar to what was discussed in section 3.1, we take a set of N evenly spaced points along z between 0 and z_{max} . For a cumulative distribution function produced from an existing data set, we can easily determine the y value for every z value, which in turn will give us N coordinates, giving $N - 1$ line segments between these co-ordinates. Now for a randomly generated y_{gen} , which lies between points $[z(n), y(n)]$ and $[z(n + 1), y(n + 1)]$, we can sample a value of z by taking the inverse of the line segment which is obtained simply by rearranging the straight line equation

$$z_{sampled} = \frac{y - c}{m}, \quad (18)$$

where $m = (y(n + 1) - y(n)) / (z(n + 1) - z(n))$ is the gradient of the line connecting two adjacent points, $c = y(n) - mz(n)$ is the intercept. This process allows for the generation of as many samples as required whilst maintaining the original cdf.

3.4. Rejection sampling

Finally, we cover another pseudo-random number sampling method, in the form of rejection sampling. With this method we can use a simple uniform number generator to sample any distribution. Consider two distribution functions, $p_1(x)$ and $p_2(x)$, where $p_1(x) > p_2(x) \forall x$. Now, we randomly sample a point, x_1 , in $p_1(x)$, and use this value to sample $y \sim U[0, p_1(x_1)]$. If $y < p_2(x_1)$, we accept the point, otherwise it is rejected. This sampling method can be slow especially if the area between the two distributions is large, since the majority of points will be rejected. This method is used for sampling objects in uniform co-moving volume (more detail in section 4.2) and produces an acceptance ratio of approximately 0.5.

4. Results

4.1. Parameter estimation using type Ia supernovae

With this numerical framework in place, it was possible to begin parameter estimation using SNeIa. A logical approach towards the generation of mock SN data was to start with a set of real data. For this, a combination of SNeIa from the Supernovae Legacy Survey with other low-redshift observations including that from the Sloan Digital Sky Survey, were used. This data set consists of 459 SNeIa observations, all with data on redshift, apparent luminosity, distance modulus, and associated errors. With this set of data it was possible to begin parameter estimation using the χ^2 minimisation method, mentioned in section 3.2. The χ^2 value is calculated with equation 12, where N is the number of supernovae, x_i and $x(\lambda)_i$ become distance moduli μ_i^{obs} and μ_i^{pred} , respectively, and σ_i is the total uncertainty for the i^{th} object. The process results in a grid of χ^2 values being calculated where the most likely combination of density parameters will result in the lowest value. This data set can be represented as a confidence plot with the contour lines representing regions of confidence.

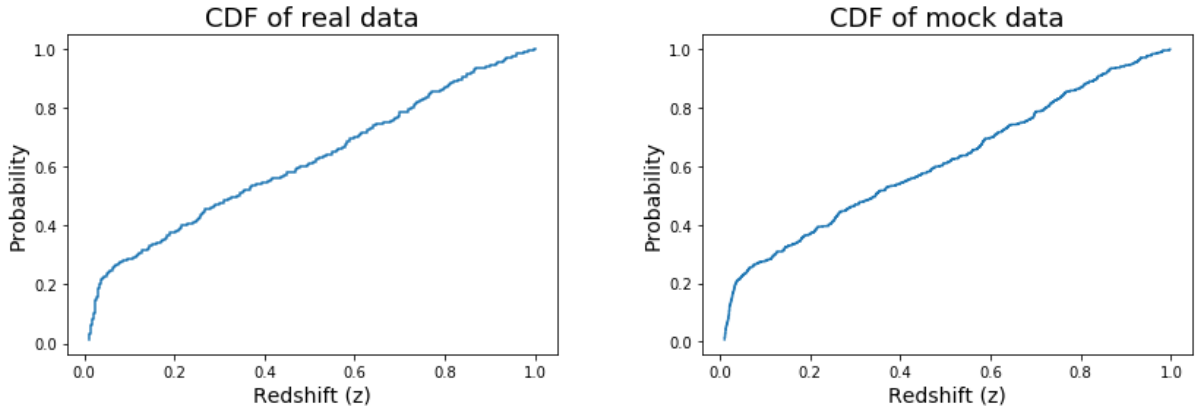


Figure 4. Comparison of cumulative distribution functions for a real data set (left) compared to a generated mock data set (right). Real data set consists of 459 SNeIa at various redshifts taken from combined data sets produced from low- z , SDSS and SNLS. Mock SNeIa is generated using the integral transform method on the real data set. Plots represent the normalised total number of counts, $n < z$, at every z point.

Now, to generate mock SNeIa data it was necessary to create a cdf of the real redshift data which would allow the mock data to be of the same distribution as the real data. Since the cdf did not have an obvious analytical inverse, we used the inverse cdf method outlined in section 3.3. This allowed us to sample as many supernovae as possible whilst maintaining the same distribution of the real data. Distance modulus was then calculated for each object and we added a corresponding error to each value by sampling the errors produced from the real data

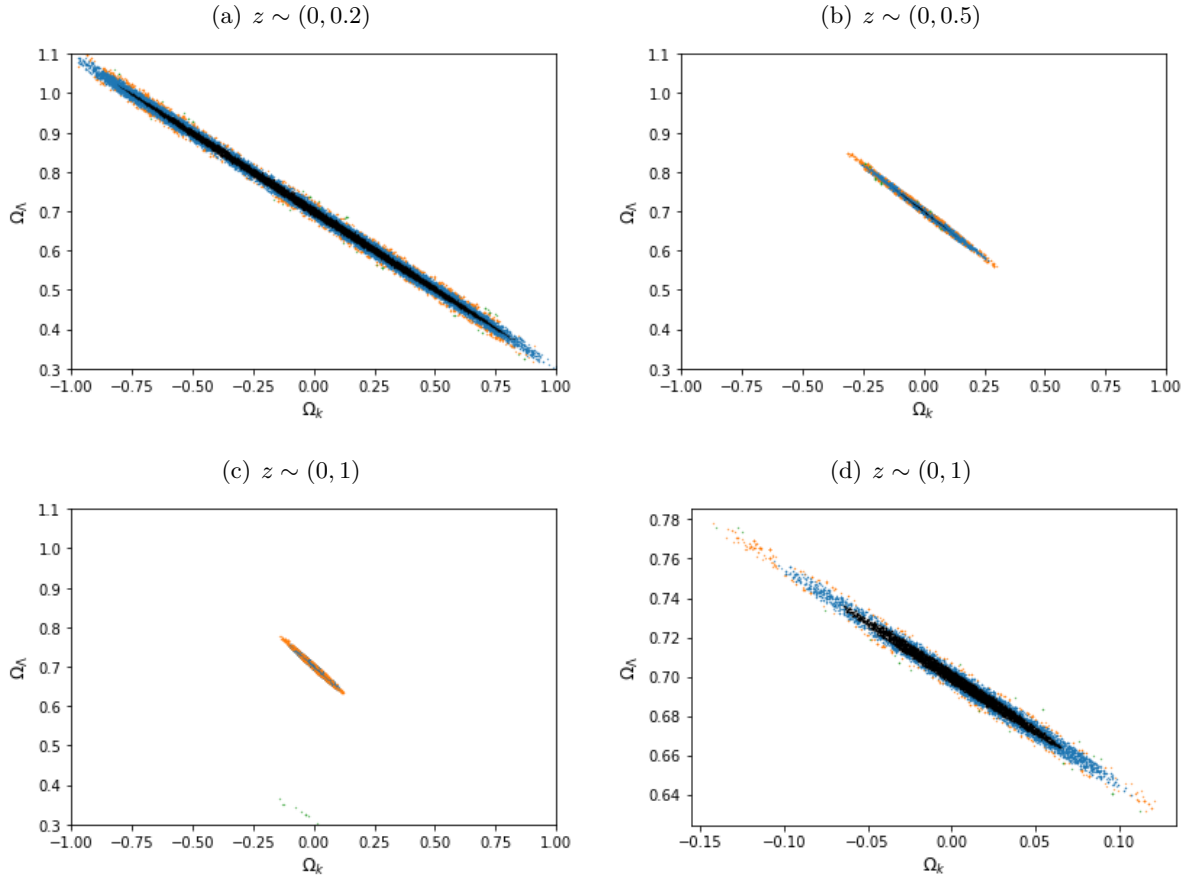


Figure 5. Confidence plots produced from 10000 SNeIa at varying redshift ranges, where black region represents parameter estimation with 68% confidence, blue with 95%, and orange with 99% (corresponding to 1σ , 2σ , and 3σ , respectively) - any points outside this region appear green. Titles indicate redshift range; (a) $z \sim (0, 0.2)$ with $\sigma_{\Omega_k} = 0.475$, (b) $z \sim (0, 0.5)$ with $\sigma_{\Omega_k} = 0.105$, and (c) $z \sim (0, 1)$ with $\sigma_{\Omega_k} = 0.041$. (d) shows a magnified $z \sim (0, 1)$.

set. It was then possible to employ the MCMC method previously discussed to analyse various constraining powers of SNeIa.

We first compared how constraining power increases from increasing the redshift range at which the supernovae are observed. It is clearly expected the larger the redshift range, the better the constraining power, however, it is interesting to see how much of an effect this has on results. We set an upper limit on this of a redshift of $z = 1$, since this is the maximum redshift expected from observations from the LSST in particular. We see that increasing the redshift range from $z = (0, 0.2)$, to $z = (0, 1)$ for 10000 SNeIa, as shown on figure 5, improves the constraints on the curvature density (for 68% confidence by a factor of ~ 10). This is largely due to the fact that higher redshifts will allow us to extrapolate different models more accurately, low redshift measurements make it hard to distinguish between varying models.

We then considered the best case scenario for redshift range and see how the number of supernovae affected the constraining power on Ω_k , as shown on figure 6. Once again we expect a larger number to yield tighter constraints, testing various constraints up to a maximum of 500000 SNeIa, which is an optimistic limit to the number of events to be observed with future detectors.

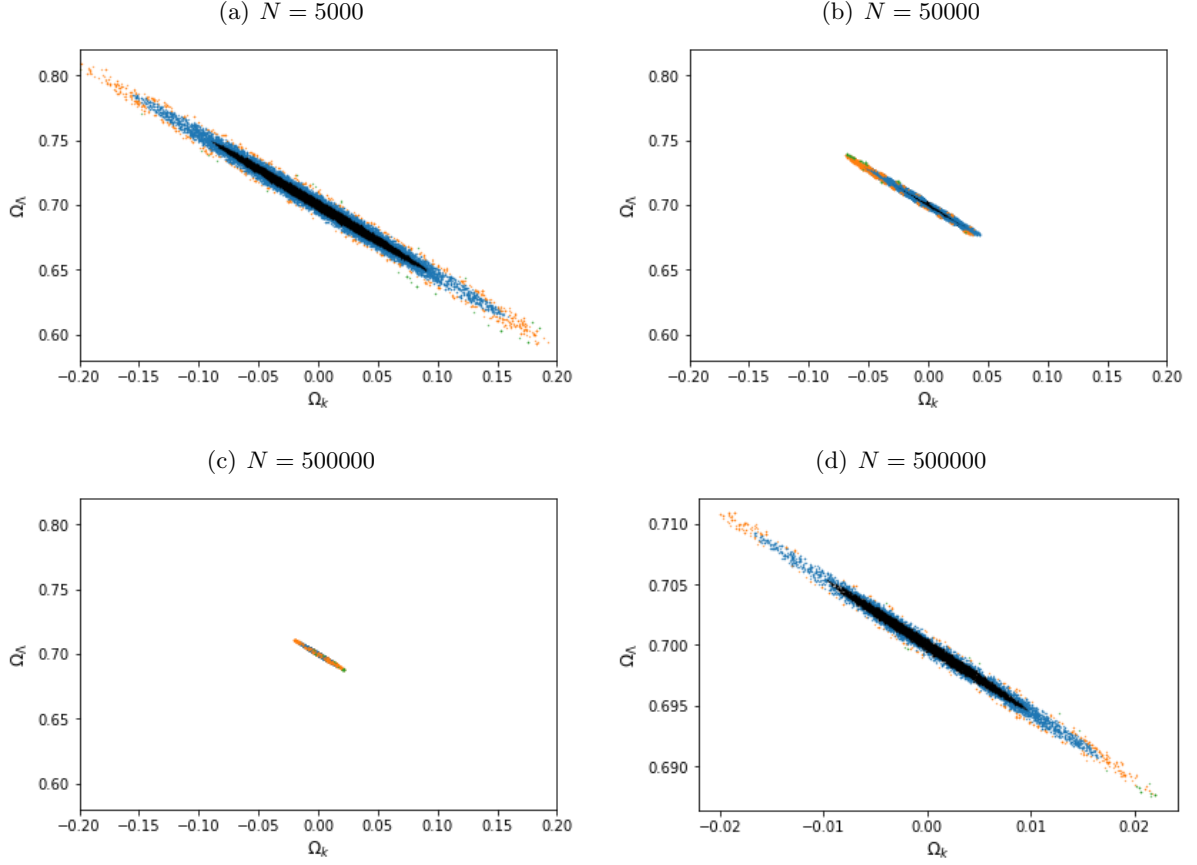


Figure 6. Confidence plots produced from a varying number, N , of supernovae at a redshift range of $z \sim (0, 1)$. (a) $N = 5000$ with $\sigma_{\Omega_k} = 0.0589$, (b) $N = 50000$ with $\sigma_{\Omega_k} = 0.0219$, and (c) $N = 500000$ with $\sigma_{\Omega_k} = 0.00671$. (d) shows a magnified $N = 500000$.

The main reason we see an increase in precision of the constraints is due to an increased sampling reducing the overall statistical biases associated with each measurement. Our upper limit constraint gives a uncertainty of $\sigma_{\Omega_k} = 0.00671$, which is still significantly larger (by a factor of ~ 3) than that provided by the CMBR. This is approaching a similar level of uncertainty, which could potentially be increased further with improvements discussed in section 5.

4.2. Parameter Estimation using massive binary black hole mergers

The process of parameter estimation using MBBHM is analogous to that of SNeIa. However, since there is no existing database for such gravitational wave observations, generating a set of observables based on current observations would be impossible. It was a sensible assumption that gravitational waves events will be uniformly distributed throughout the Universe, thus the events can be distributed in uniform co-moving volume. For this process, rejection sampling was used as described in section 3.4. This involved using the co-moving distance formula, equation 6, to calculate the upper and lower bounds of co-moving distance depending on the redshift range the object are being generated over. Using these we could generate a uniform number in the range, $[-d_c(z_{max}), d_c(z_{max})]$, for all x, y and z directions. Taking the magnitude of these combined components, we could reject specific numbers if they lie outwith the range, $[d_c(z_{min}), d_c(z_{max})]$, and then use an inverse sampling method to obtain the corresponding redshift.

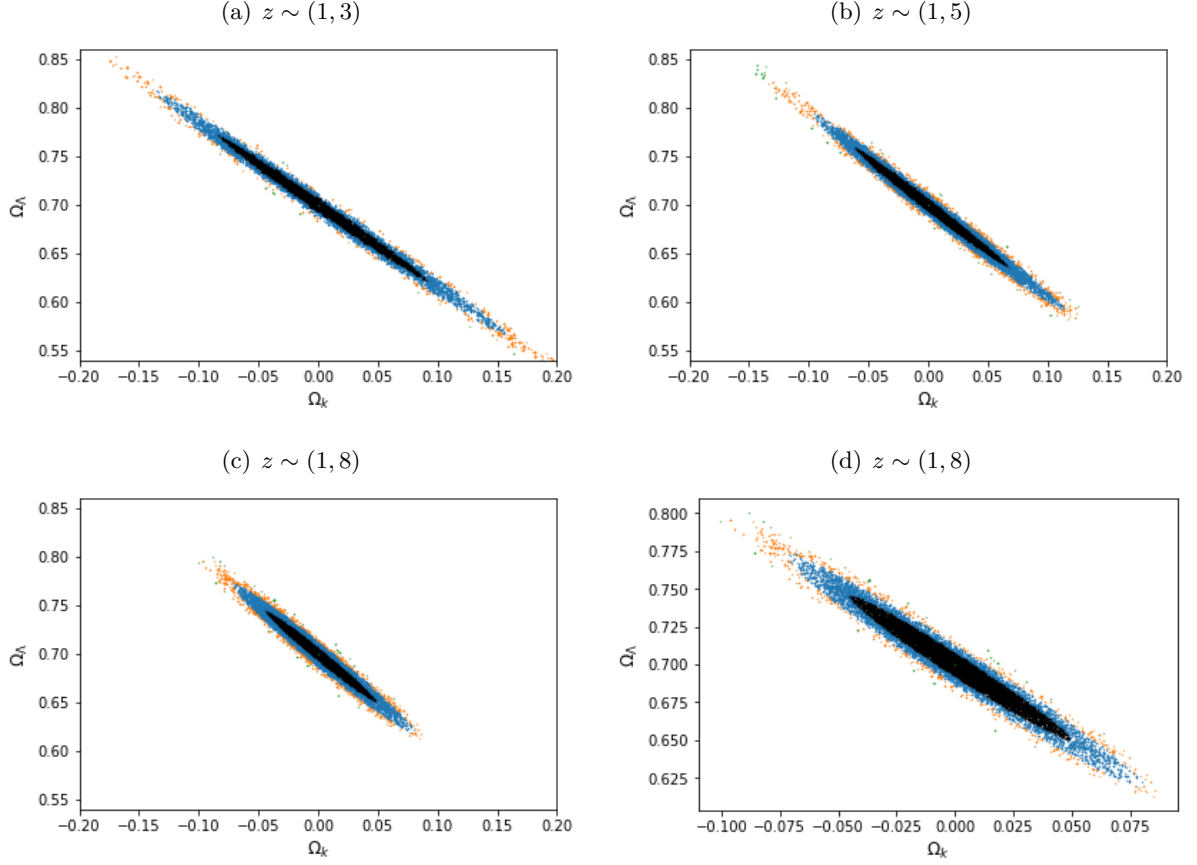


Figure 7. Confidence plots produced from 100 MBBHM at varying redshift ranges. (a) $z \sim (1, 3)$ with $\sigma_{\Omega_k} = 0.063$, (b) $z \sim (1, 5)$ with $\sigma_{\Omega_k} = 0.0425$, and (c) $z \sim (1, 8)$ with $\sigma_{\Omega_k} = 0.0288$. (d) shows a magnified $z \sim (1, 8)$.

After the points had been generated, the same process used for the supernovae was repeated for calculating the luminosity distance, and in turn, the distance modulus. The intrinsic error for the luminosity distance is significantly less than that of supernovae since we understand the mechanism behind the production of gravitational waves from MBBHM well. However, we cannot simply ignore the effect of gravitational weak lensing especially since the objects are being observed to a much larger redshift. We thus extrapolated the results from Shapiro *et al.* (2009) [12], to produce errors on each object. Details of the production of these errors are covered by Wang *et al.* (2002) [13]. Once again we compare the result from varying redshift range, setting an upper limit of $N = 100$, and $z \sim (1, 8)$, respectively. The upper limit of objects expected to be observed is used to allow for the redshift distribution to be sampled as evenly as possible.

It can be seen, on figure 7, that varying redshift range makes less of a difference when compared to slightly increasing the range for SNIa. This is likely due to the fact that from redshift $z = 1$ we can already largely distinguish models, thus extrapolating further will make less difference.

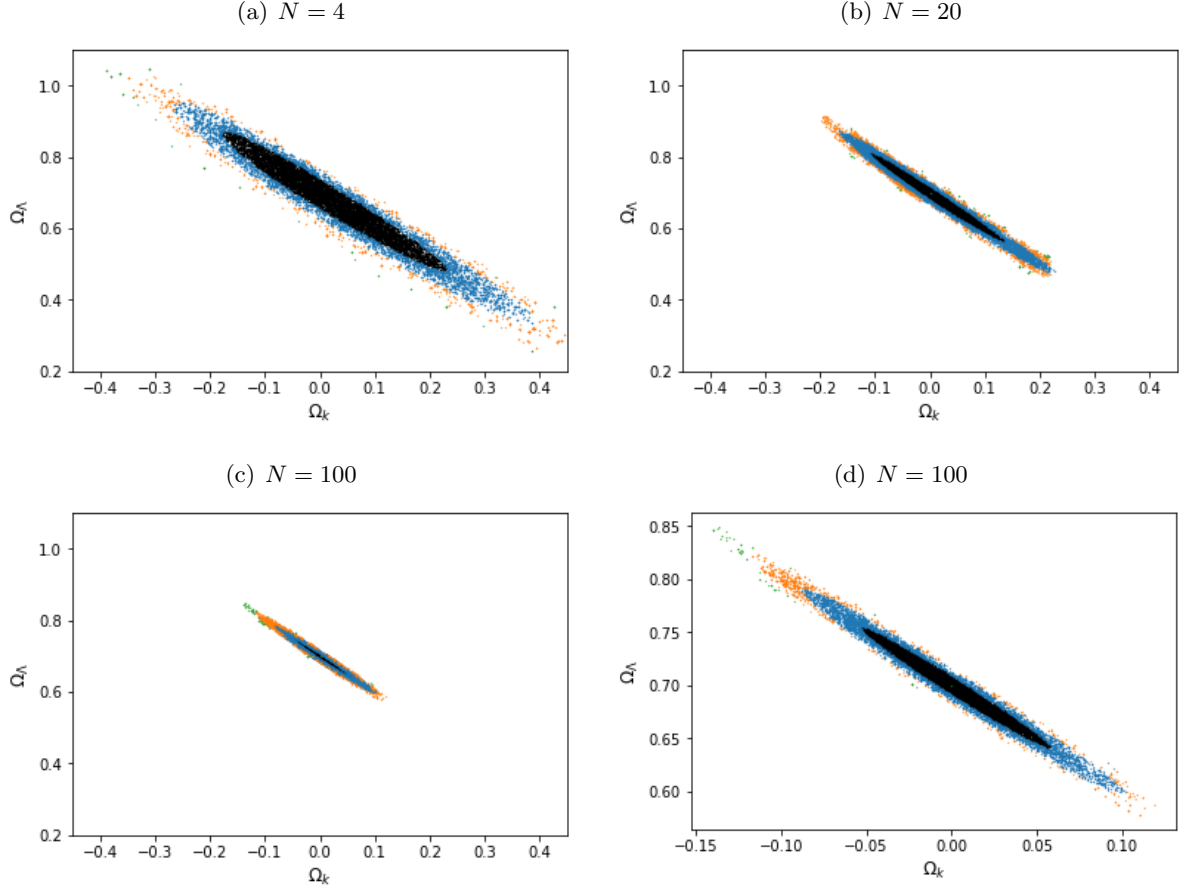


Figure 8. Confidence plots produced from a varying number of MBBHM at a redshift range of $z \sim (1, 8)$. (a) $N = 4$ with $\sigma_{\Omega_k} = 0.133$, (b) $N = 20$ with $\sigma_{\Omega_k} = 0.0791$, and (c) has $N = 100$ with $\sigma_{\Omega_k} = 0.0288$. (d) shows a magnified $N = 100$.

Next, we look at the effect of varying the number of MBBHM, as shown in figure 8. Just 100 MBBHM over a redshift range $z \sim (1, 8)$ provide better constraints than 10000 SNeIa. We achieve a maximum constraint after reducing the errors from gravitational weak-lensing (figure 9) of $\sigma_{\Omega_k} = 0.0165$, still a factor of ~ 10 larger than the CMBR. It is noted here that Gaussianity is assumed for the magnification due to weak-lensing. Despite it not being Gaussian, this is a valid approximation especially when we consider a larger number of objects. The central limit theorem backs this up, stating that the sum of any independent variables will tend towards a normal distribution.

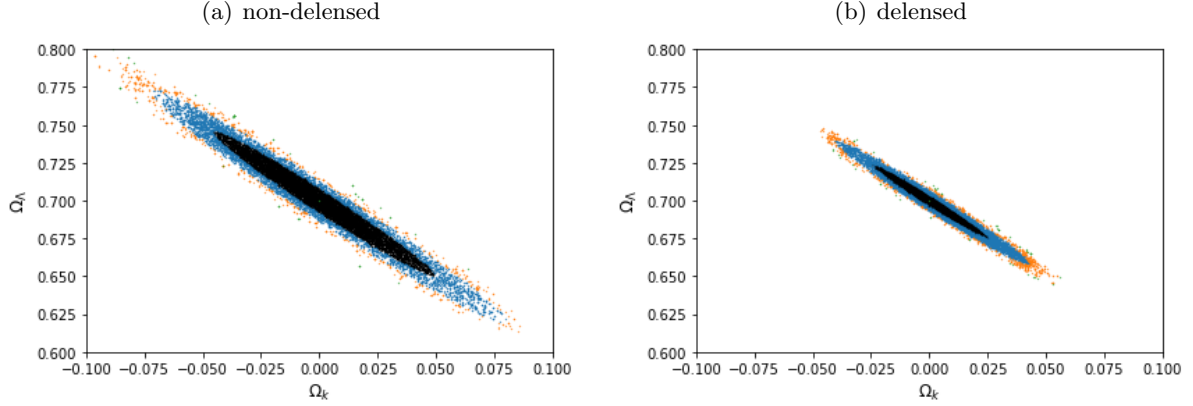


Figure 9. Confidence plots comparing the affect of correcting for gravitational weak lensing. Produced from 100 MBBHM at a redshift range of $z \sim (1, 8)$, (a) shows non-delensed with $\sigma_{\Omega_k} = 0.0288$ and (b) shows delensed with $\sigma_{\Omega_k} = 0.0165$, almost a factor of two increase in precision.

4.3. Combining SNeIa and MBBHM

Combining the constraints from the two probes offers potential for further refinement. Looking at the upper limit of possible observations expected and combining both results from both SNeIa and delensed MBBHM will give us a good understanding of the best constraints we can get from future probes. Figure 10, shows an error on the curvature density of $\sigma_{\Omega_k} = 0.0036$. The complementary redshift range between both SNeIa and MBBHM result in tight constraints on the curvature density to almost the same level predicted by the CMBR.

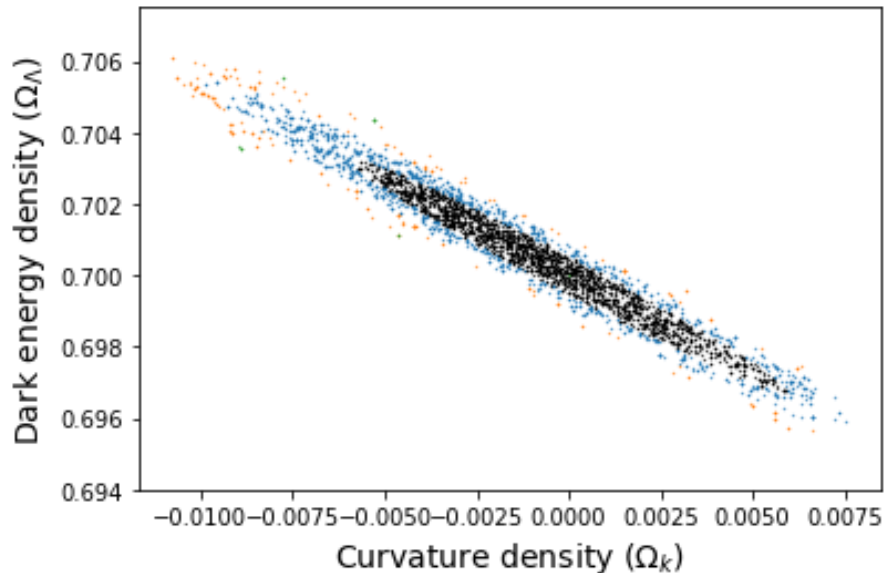


Figure 10. Confidence plots from combining 500000 SNeIa, $z \sim (0, 1)$, and 100 delensed MBBHM, $z \sim (1, 8)$. $\sigma_{\Omega_k} = 0.0036$, a factor of ~ 2 larger than the CMBR.

5. Future Work

5.1. Further SNeIa and BBHM searches

This project has focused on the use of SNeIa and MBBHM solely from predicted observations from LSST and LISA respectively. There are, however, many other future missions forecast for the observation of these probes, and since forecasts using the LSST and LISA data appear not to constrain the curvature parameter to the level of the CMBR, using results from more surveys will increase precision of parameter estimation further. One such mission is the Dark Energy Survey - which expects to observe 4000 SNeIa up to a redshift of $z = 1.2$ [14]. Despite the number seeming quite insignificant compared to LSST observations, all redshift measurements will be spectroscopic which provides vanishingly small errors on redshift values along with the increased redshift range (which has been shown to have significant impact on the constraints provided), thus could provide the extra constraining power to achieve a similar variance level to that of the CMBR. Both the Extremely Large Telescope and the James Webb space telescope have capabilities of observing supernovae up to a redshift of $z \sim 4$, once again, the large redshift range could provide extra necessary constraints.

For further BBHM searches we can include the Deci-hertz Interferometer Gravitational wave Observatory and the Einstein Telescope, which combined will hugely increase the frequency range at which coalescing binaries can be observed.

5.2. Combining with other probes

As mentioned before, we have many cosmological probes to constrain cosmological parameters. One hugely promising probe is that of BAOs, especially when combined with SNeIa and BBHM. This is largely due to the fact that SNeIa measurements are calibrated against the Hubble flow, whereas BAO measurements are made from well understood physical principles directly extrapolated from the CMBR. Hence, the combination of relative, and absolute measurements along with the fact that the two probes have almost entirely different systematic uncertainties, result in highly complementary constraints. On top of this the sheer amount of SNeIa observations made by LSST will allow statistical peaks in the 2-point correlation function to be observed - the method for observing BAO.

Promise also lies with the use of stellar mass BBHM without the need for redshift measurements which is covered in Ding *et. al.* (2018) [15], which describes purely the use of luminosity distance and the prior knowledge of redshift distributions of BH-BH mergers. 10^5 of these observations are expected to give 1% constraints on H_0 , which is an optimistic expectation since we can only expect $\sim 10^4$ events from LISA.

Finally we can look at redshift drift as a new probe for constraining cosmological parameters. This process involves obtaining the spectrum of an object, then comparing it to the spectrum from the same object several years later [16]. This gives precise measurements of the local Hubble parameter for the object, and can be used in synergy with other probes to determine the curvature parameter.

5.3. Different models

Another interesting approach for the project to take would be how this data could be used to estimate parameters in a different cosmological model. This project assumes a Λ CDM model, however, there are many other cosmological models which also accurately describe the Universe such as conformal gravity theories, which suggests that gravity becomes repulsive at large enough scales, and the evolving equation of state model, in which the equation of state describing dark energy is no longer constant and varies throughout the evolution of the Universe. Using the same data set, we could determine how well parameters in these models could be constrained, and follow up by using a Bayesian odds ratio method to see which one of the models proves most likely.

5.4. Improved sampling

In this project we assume that the distributions have successfully converged to the target distribution. There are possible techniques which could be implemented to help check for, and increase, convergence. For example, using a “burn in”, which eliminates the first few guesses in the chain. This results in minimising the effect of a bad choice of starting point in the parameter space - which will have minimal impact on data generated for this project since we have chosen the point of maximum likelihood as the initial starting point. Thinning of the data set could be used, taking only every predefined n^{th} value, which will reduce auto-correlation of the samples. This means that it will decrease the overall impact of the chain getting “stuck” in a specific area of the parameter space, but also has the negative effect of reducing the sample size by a factor of n thus increasing computational time to achieve a required sample size. Proposal density is an important factor, as mentioned in section 3.2. One suggestion for optimising the proposal density would be by having it set as a function of the acceptance ratio, if the ratio is low (proposal density is too high) we can decrease the value of the proposal density until a more desirable acceptance ratio is achieved and vice-versa for too high an acceptance ratio. Finally and probably most importantly, multiple runs could be used. This is important to ensure the samples have converged to the posterior, and can be confirmed by visually comparing multiple runs. It will also allow for a better estimation of the error on Ω_k , since we can take an average over multiple runs.

6. Conclusion

This project has successfully demonstrated the constraining power of type Ia supernovae and massive binary black hole mergers as cosmological probes. MBBHM are excellent probes with relatively small associated errors resulting in high constraints with only a few observations. This comes with the limitation that only a small number are likely to be observed when compared to the hundreds of thousands of supernovae. The constraints provided independently by the two probes are significantly larger than that achieved by observations of the CMBR, however, the combination of the two probes come very close - largely due to their highly complementary redshift ranges.

Future observations are likely to constrain the spatial curvature parameter to a high precision almost to the same level of variance predicted by the CMBR, and with suggested improvements mentioned, this level could even be surpassed. With this increased precision we have the large potential for distinguishing between different geometries of the Universe, in the case of it only deviating slightly from a flat universe, we can say with confidence that our observable universe is only a small part of a much larger universe. However, taking the curvature density of $\Omega_k = 0.001$ predicted by the CMBR, this seems unlikely with current prospects. Nonetheless, this method will provide tight constraints independent of those provided by the CMBR, which may give us confidence in our current model, or even more exciting, tell us we need to look elsewhere for a better description of our universe.

7. Acknowledgements

I would like to give a special thanks my supervisor, Professor Martin Hendry, for his invaluable advice and guidance throughout the course of my project. Also thanks to members of and those working with the Institute for Gravitational Research at the University of Glasgow for insightful discussions.

8. References

- [1] J. A. Frieman, M. S. Turner, and D. Huterer. Dark Energy and the Accelerating Universe. , 46:385–432, September 2008.
- [2] S. Perlmutter et al. Measurements of Ω and Λ from 42 High-Redshift Supernovae. , 517:565–586, June 1999.
- [3] B. P. Schmidt, A. G. Riess, et al. The High-Z Supernova Search: Measuring Cosmic Deceleration and Global Curvature of the Universe Using Type IA Supernovae. , 507:46–63, November 1998.
- [4] Planck Collaboration, N. Aghanim, et al. Planck 2018 results. VI. Cosmological parameters. *arXiv e-prints*, page arXiv:1807.06209, Jul 2018.
- [5] D. Huterer and D. L. Shafer. Dark energy two decades after: observables, probes, consistency tests. *Reports on Progress in Physics*, 81(1):016901, January 2018.
- [6] B. Abbott et al. Observation of gravitational waves from a binary black hole merger. *Phys. Rev. Lett.*, 116:061102, Feb 2016.
- [7] Chris Pankow, Eve A. Chase, Scott Coughlin, Michael Zevin, and Vassiliki Kalogera. Improvements in Gravitational-wave Sky Localization with Expanded Networks of Interferometers. , 854:L25, Feb 2018.
- [8] LSST Dark Energy Science Collaboration. Large Synoptic Survey Telescope: Dark Energy Science Collaboration. *arXiv e-prints*, page arXiv:1211.0310, Nov 2012.
- [9] Amaro-Seoane et al. Laser Interferometer Space Antenna. *arXiv e-prints*, page arXiv:1702.00786, Feb 2017.
- [10] David W. Hogg. Distance measures in cosmology. *arXiv e-prints*, pages astro-ph/9905116, May 1999.
- [11] L. Verde. *Statistical Methods in Cosmology*, pages 147–177. 2010.
- [12] C. Shapiro, D. J. Bacon, M. Hendry, and B. Hoyle. Delensing gravitational wave standard sirens with shear and flexion maps. , 404:858–866, May 2010.
- [13] Yun Wang, Daniel E. Holz, and Dipak Munshi. A Universal Probability Distribution Function for Weak-lensing Amplification. , 572:L15–L18, Jun 2002.
- [14] I. M. Hook. Supernovae and cosmology with future European facilities. *Philosophical Transactions of the Royal Society of London Series A*, 371:20120282–20120282, Apr 2013.
- [15] Xuheng Ding, Marek Biesiada, Xiaogang Zheng, Kai Liao, Zhengxiang Li, and Zong-Hong Zhu. Cosmological inference from standard sirens without redshift measurements. *arXiv e-prints*, page arXiv:1801.05073, Jan 2018.
- [16] Raul Jimenez, Alvise Raccanelli, Licia Verde, and Sabino Matarrese. Peering beyond the horizon with standard sirens and redshift drift. *Journal of Cosmology and Astro-Particle Physics*, 2018:002, Apr 2018.